

Quantum metric and localization in a quasicrystal

Quentin Marsal,* Patric Holmval, and Annica M. Black-Schaffer

Department of Physics and Astronomy, Uppsala University, Box 516, 751 20 Uppsala, Sweden

(Dated: June 19, 2025)

We use the quantum metric to understand the properties of quasicrystals, represented by the one-dimensional (1D) Fibonacci chain. We show that the quantum metric can relate the localization properties of the eigenstates to the scale-invariance of both the chain and its energy spectrum. In particular, the quantum metric incorporates information about distances between the local symmetry centers of each eigenstate, making it much more sensitive to the localization properties of quasicrystals than other measures of localization, such as the inverse participation ratio. We further find that a full description of localization requires us to introduce a new phasonic component to the quantum metric, and a mixed phason-position Chern number. Finally, we show that the sum of both position and phasonic components of the quantum metric is lower-bounded by the gap labels associated with each energy gap of the Fibonacci chain. This establishes a direct link between the spatial localization and fractal energy spectrum of quasicrystals. Taken together, the quantum metric provides a unifying, yet accessible, understanding of quasicrystals, rooted in their scale-invariance and with intriguing consequences also for many-body physics.

I. INTRODUCTION

Quasicrystalline materials have since their experimental discovery in 1984 [1] been subject to growing interest thanks to their highly peculiar electronic properties. Quasicrystals are long-range ordered materials like crystals, but without translation symmetry. Instead, the long-range order in quasicrystals stems from scale-invariance of their atomic structure, visible in their diffraction pattern [1]. Consequently, the emergent electronic properties of quasicrystals are closely related to their unusual atomic structure. Recent studies have in particular focused on the localization properties of the electronic states, demonstrating their criticality [2] and topological properties [3–7]. There is also growing interest in how these localization properties influence interacting [8, 9] and ordered states such as superconductivity [10–16] or its proximity effect [17, 18] and Josephson effect [19], topological superconductivity [20–23], and antiferromagnetism [24]. Recently, quasiperiodicity has also been found in moiré structures [25–28], further broadening the importance of quasicrystals.

Among the most studied quasicrystals is the Fibonacci chain [29]. It is a chain of sites (atoms) coupled by two types of hoppings that alternate following a regular, but non-crystalline pattern. Since it is one-dimensional (1D), it is simple to study and both numerical and analytical results of the electronic spectrum are available [30–33]. Yet, it remains similar to more elaborate quasicrystals, as it exhibits most of the general properties of quasicrystals [14, 34, 35], including the effect of hidden dimensions [36–38]. It has therefore come to serve as an effective model to describe the essential physics of also 2D and 3D quasicrystals [14, 29, 34]. Moreover, the Fibonacci chain has been experimentally realized and studied in a wide range of physical systems [3, 35, 39–47].

Stemming directly from the quasicrystalline nature of the Fibonacci chain, the localization properties of its electronic eigenstates are key for understanding its physics [48]. However, so far studies have been mainly restricted to using the

inverse participation ratio (IPR) [49] or multifractal exponents [35, 50, 51], which only give a partial description of localization and also do not provide any direct relationship to the energy spectrum. Indeed, these indicators only take into account the number of occupied sites for a given state and thus do not capture correlations of the localization of the electronic state to the local atomic structure of the chain, known to produce scale-invariance and multifractal states [35, 50].

In this work, we establish the quantum metric as an indispensable and natural tool for providing extensive understanding of quasicrystals, capturing both their intricate localization properties and their relation to the energy spectrum. The quantum metric measures distances between eigenstates based on a parameter space, usually momentum space [52]. It has also been proven to have a simple interpretation in real space, where it gives the localization of Wannier orbitals [53]. Building on the quantum metric efficiently probing localization, we have in a recent work shown that disorder may enhance the quantum metric [54] when the impurity states are critically localized. In addition, the quantum metric has recently been found to be important for interacting properties of narrow or flat bands, for example by enabling superconducting phase coherence [55, 56] and the fractional quantum Hall effect [57–59].

The ability of the quantum metric to measure localization and its relation to long-range phase coherence makes it an interesting tool for quasicrystals. To this end, we explore how the quantum metric can quantify localization properties of the Fibonacci chain. By showing how the quantum metric incorporates information about distances between local symmetry centers of each eigenstate and how these are inherently linked to the scale-invariance of the Fibonacci chain, we are able to establish a direct correspondence between the structural properties of the chain and the localization of its electronic states as measured by the quantum metric. The quantum metric thereby provides a well-refined measure of electronic localization, directly rooted in the scale-invariance of the chain. This makes the quantum metric a natural tool for understanding localization in general quasicrystals, also beyond the 1D Fibonacci chain, in contrast to the IPR and related tools that primar-

* quentin.marsal@physics.uu.se

ily focus only on the number of occupied sites [35, 49, 50]. Moreover, with the quantum metric being a numerically easily accessible observable, with rapidly emerging experimental signatures [60–62], it offers direct access to electronic localization of quasicrystals.

We also introduce a novel formulation for the quantum metric that in addition takes into account the different phason modes, encoding different incarnations of the chain, as an independent degree of freedom. We show that the full quantum metric, defined as the sum of the spatial and phasonic quantum metric contributions, inherits properties from those of a 2D crystal. Importantly, we are able to provide a lower bound of the full quantum metric, set by the Chern number of the 2D crystal. Since the same Chern number labels the gaps in the energy spectrum of the quasicrystal [36], we can explicitly relate the full quantum metric to the fractality of the energy spectrum in quasicrystals. For weak quasicrystal modulations we show numerically that the spatial quantum metric tightly follows this lower bound, thus explicitly linking spatial localization to the energy spectrum and its fractal gap structure. These results also establish that quasicrystals are materials where the quantum geometry can be tuned over a wide range. This opens for many-body phases in quasicrystals dependent on the quantum metric, such as flat-band superconductivity [55, 56] and fractional quantum Hall effect in Chern insulators [57–59].

Below we report our results, starting with the construction of the Fibonacci chain in Section II, followed by a study of its localization properties in Section III in terms of local density of states and the IPR. Then in Section IV we introduce the quantum metric and calculate it for the Fibonacci chain. In Section V we provide an understanding of the superiority of the quantum metric for understanding localization in a quasicrystal by analyzing how the chain is build up by local symmetry centers. Then in Section VI we expand the spatial quantum metric with a phasonic component and are thus able to derive a hard lower bound that explicitly links the full quantum metric to a higher dimensional Chern number, and thereby the energy spectrum properties. Finally, in Section VII we summarize our results and highlight their generality.

II. CONSTRUCTING A FIBONACCI CHAIN

The Fibonacci chain is a 1D quasicrystal made of a specific combination of two types of nearest-neighbor hopping terms t_L and t_S , corresponding to long (L) and short (S) bonds, respectively, that alternate in a long-range ordered but non-crystalline manner [29] with the Hamiltonian

$$\mathcal{H} = \sum_n t_n c_n^\dagger c_{n+1} + \text{H.c.}, \quad (1)$$

where n enumerates all sites in a finite chain. This work considers the localization properties of the resulting electronic eigenstates and their relation to the spectrum of the energy eigenvalues, solved by exact diagonalization. Although we only consider a Fibonacci chain with hopping modulation, equivalent results can be obtained for onsite modulations using an established mapping [36].

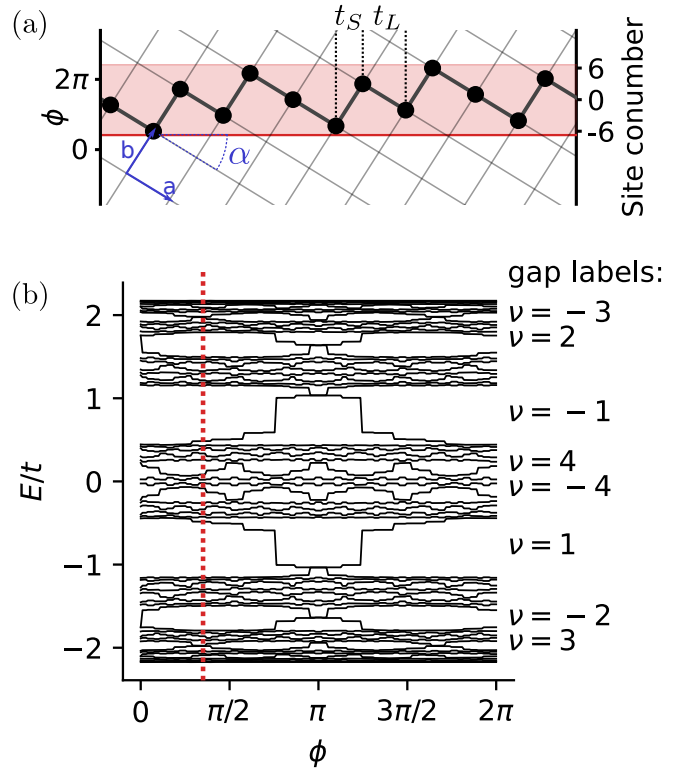


Figure 1. (a) Construction of a 13-site long periodic approximant of the Fibonacci chain by the cut-and-project method. The approximant is obtained by projecting a square lattice on the red horizontal line along the x direction. The slope of this line cut, here $5/8$, determines the length of the approximant. The vertical, y -axis, intercept of the line-cut determines the phasonic mode ϕ , see left y -axis. Bonds along the a -axis project onto the horizontal line as long (L) bonds, while bonds along the b -axis project as short (S) bonds. Sites can also be labeled by their conumber, obtained by projection on the orthogonal, y -axis, see right y -axis. Sites with close conumbers have similar local environments. (b) Energy spectrum obtained for the full range of phasonic modes ϕ under OBCs. The spectrum acquires edge modes that wind through the energy gaps as a function of ϕ . Gaps are labeled based on this winding number ν . Dashed red line shows the spectrum for the phason mode drawn in (a).

The quasicrystalline sequence of hopping terms (t_n) results from successive concatenations of longer and longer approximants, following the Fibonacci recursion relation. The two shortest, trivial, approximants are $F_0 = t_S$ and $F_1 = t_L$, and then with all others obtained through $F_n = F_{n-2}F_{n-1}$. Thus, the shortest non-trivial approximants are

$$F_2 = t_S t_L, \quad (2)$$

$$F_3 = t_L t_S t_L, \quad (3)$$

$$F_4 = t_S t_L t_L t_S t_L, \quad (4)$$

$$F_5 = t_L t_S t_L t_S t_L t_L t_S t_L, \quad (5)$$

$$\text{etc.} \quad (6)$$

This recursive construction makes the Fibonacci chain scale invariant. For example, F_2 appears three times in F_5 , F_3 appears twice, and F_4 once. The scale-invariance is also seen

from the fact that each approximant can be obtained from the previous, shorter one using the inflation rules [29]

$$t_S \rightarrow t_L, \quad (7)$$

$$t_L \rightarrow t_S t_L. \quad (8)$$

As a direct consequence, the Hamiltonian, and thus the energy spectrum and wave functions, also become scale invariant.

Approximants can alternatively be built using the 'cut-and-project' method [63], which emphasizes the long-range structure of the chain. It consists of cutting a stripe from a tilted 2D square lattice, and projecting the sites it contains onto a 1D line, as illustrated in Fig. 1(a). When projected along the line-cut direction, the bonds along the a -axis result in long bonds t_L , whereas bonds along the b -axis project as short bonds t_S . The slope of the tilted square lattice, $\tan(\alpha)$, entirely determines the obtained chain: rational slopes correspond to periodic chains, while irrational slopes give rise to true quasicrystals. The Fibonacci chain corresponds to a slope equal to the golden mean $\tan(\alpha) = \frac{1+\sqrt{5}}{2}$. Rational slopes close to this ratio lead to the approximants (F_n).

The 'cut-and-project' method has the benefit that projecting sites along the perpendicular direction to the line cut, *i.e.* vertical axis in Fig. 1(a), allows us to associate a so-called conumber to each site, based on its vertical position. The conumber reflects the local environment of each site, with sites with close conumbers sharing similar local environments and sites with opposite conumbers having mutually symmetric local environments [32, 64]. In the example shown in Fig. 1(a), the approximant contains 13 sites, with sites thus conumbered from -6 to 6 . Sites with conumber between -6 and -2 have a long bond on their left and a short bond on their right, whereas the opposite is true for sites with conumbers between 2 and 6 . All these sites form pairs around a strong t_S bond and can therefore be called molecular sites. Sites with conumbers -1 , 0 , and 1 sit in-between long bonds. Those sites thus become isolated in the strongly modulated limit, $t_L \ll t_S$, and can therefore be called atomic sites [14].

The sequence of hopping terms obtained by the 'cut-and-project' method in fact depends on the y -intercept of the line cut, which can be labeled by the so-called phason parameter, or angle, ϕ . One can therefore rewrite a general Eq. (1) as

$$\mathcal{H}(\phi) = \sum_n t_n(\phi) c_n^\dagger c_{n+1} + \text{H.c.}, \quad (9)$$

where the explicit dependence of t_n on ϕ reads [29]

$$t_n(\phi) = \frac{t_L + t_S}{2} (1 + \delta \operatorname{sgn}[\cos(2n\pi \tan(\alpha) + \phi) - \cos(\pi \tan(\alpha))]), \quad (10)$$

with $\delta = \frac{t_S - t_L}{t_L + t_S}$ quantifying the modulation strength of the chain. Equation (10) shows that a shift in ϕ is equivalent to a shift of the site position n and can thus be discarded by a change of the origin of positions. This makes the phason parameter irrelevant under periodic boundary conditions (PBCs). However, under open boundary conditions (OBCs) different phason parameters boil down to opening the chain at different sites,

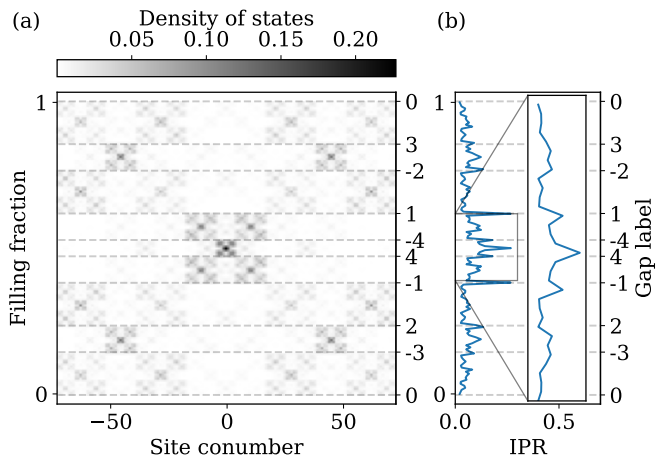


Figure 2. (a) Local density of states map of the eigenstates of the 144-site long Fibonacci approximant F_{11} with modulation strength $\delta = 0.5$, averaged over the different phason modes. Eigenstates are sorted by increasing filling fraction on the vertical y -axis, and sites are sorted by local environment, according to their conumber, along the x -axis. Dashed grey lines shows the position of the main energy gaps of the spectrum, along with their gap label on the right y -axis. (b) IPR of the eigenstates, averaged over the phason modes. Inset shows a zoom-in of the middle band to highlight the self-similar structure of the IPR.

and thus, with different terminations. Depending on the termination, edge states may form in the energy gaps between bands of energy states of the PBC chain [65]. Note that bands here designate the ranges of energy in which the eigenstates lie, but there is no dispersion relation as found in periodic systems. We illustrate this in Fig. 1(b) by plotting the energy spectrum as a function of the phason parameter. Clear gaps are identified in the spectrum. As ϕ sweeps over the different phason modes, the edge states wind within these gaps [64]. This winding of the edge states can be understood based on an analogy between quasicrystals and higher-dimensional topological insulators [3, 36–38], that we detail in Section VI. Thanks to this analogy, the energy gaps under PBCs can be labeled according to the winding number ν of the edge states inside each gap, as indicated in Fig. 1(b). This gap label can also be determined analytically based on the integrated density of states [66]. It is worth noting that gaps with higher winding numbers ν are smaller. This implies that the edge states winding in those gaps penetrate deeper in the bulk compared to edge states in larger gaps, which have smaller (absolute valued) gap labels. Thus, longer approximants are necessary to correctly resolve the narrowest gaps.

III. LOCALIZATION AND INVERSE PARTICIPATION RATIO

The scale-invariant structure of the Fibonacci chain constrains the localization properties of its eigenstates. The eigenstates of the chain can neither be fully localized, nor Bloch wave delocalized. Instead, they have been observed to be mul-

tifractal [35]. The inverse participation ratio (IPR) is a widely used tool to quantify the degree of localization of a quantum state [35, 67, 68]. In this section, we discuss the interest and limits of this indicator for the Fibonacci chain.

We start by plotting the local density of states of the 144-site approximant F_{11} in Fig. 2(a). Each horizontal line represents the local density of states of a single band in Fig. 1(b), sorted by increasing energy and averaged over phason modes. The main gaps of the system are marked by the dashed gray lines, along with the corresponding gap labels on the right vertical axis. On the horizontal axis, sites are ordered based on their conumber, *i.e.* sorted by similar local environment. Clearly, the energy gaps separate groups of states living on different sites. For example, the gaps 1 and -1 separate a central band, localized on atomic sites and hence with conumbers in the middle, from two molecular bands resulting from the hybridization of molecular sites and hence with low and high conumbers. The same structure, with gaps separating distinct clusters of states, remains true for the narrower gaps that appear deeper in the structure of the spectrum, and even for those narrower gaps not indicated by dashed lines in Fig. 2(a). In fact, each band itself decomposes into sub-bands separated by multiple smaller gaps, where each group of bands are more similar to each other. Overall, this results in an emergent fractal structure of the localization of the eigenstates along the chain.

The localization of the eigenstates in the Fibonacci chain has previously often been captured by the IPR [67]. The IPR is defined for each eigenstate $|\psi\rangle$, as $\text{IPR}(|\psi\rangle) = \sum_{\text{sites } i} |\langle i|\psi\rangle|^4$. It can intuitively be interpreted as the expectation value of the inverse number of sites on which a given state is localized. It therefore ranges from 0 for a state with equal amplitude on every site of an infinite system, *i.e.* fully delocalized, to 1 for a state fully localized on a single site. It has therefore been proven to be a useful tool to study the localization properties of eigenstates [51, 67].

In Fig. 2(b) we plot the IPR of the eigenstates of the approximant F_{11} . The fractality of the eigenstates is apparent in the profile of the IPR. Indeed, the inset highlights the self-similarity of the IPR profile as a function of filling fraction, when zooming in on the central atomic band. The IPR can also be used to distinguish localized edge states from bulk states. Indeed, the IPR profile in Fig. 2(b) shows plateaus separated by high peaks. Comparing this profile to the local density of states in Fig. 2(a), we see that the plateaus correspond to bands of fractal bulk states localized on the same groups of sites, and hence the IPR is similar for these states. The peaks, in contrast, coincide exactly with the dashed gray lines, marking the energy gaps in the system, and therefore corresponding to localized edge states. Since we plot the IPR as a function of filling fraction, the oscillating energies of the edge states across the gaps as a function of ϕ is not discernable. We also notice that the edge state peak height decreases for higher (absolute valued) gap labels. This signals that in the largest gaps, the edge state is sharply localized at the boundary. In contrast, for narrower gaps, corresponding to higher gap labels, the edge states penetrate deeper in the bulk. As a consequence, the distinction between bulk and edge states progressively fades

away for larger gap labels in the IPR. In addition, comparing Figs. 2(a,b), both averaged over the different phason modes, it is interesting to note that the localized edge states remain clearly visible in the profile of the IPR in (b), whereas they cannot be distinguished from the bulk states when plotting the local density of states in (a). This comes from the fact that the site conumber on the horizontal axis of Fig. 2(a) does not retain any information about how close a given site is to the system's edge, as this varies between different phason modes.

Based on the results in Fig. 2, we find that the IPR is a powerful tool to distinguish between fractal bulk states and localized edge states and it also captures the self-similarity in the density of states of a quasicrystal. However, it is not an appropriate tool to differentiate between bulk states belonging to different bands, which is crucial for understanding the structure of the Fibonacci chain. For example, the band located between gap labels -3 and 2 and the one between -1 and 4 are located at very different local environments: the former is localized on molecular sites, whereas the latter occupies atomic sites, as easily seen by their conumbers. But they still occupy a similar number of sites, and thus the IPR cannot distinguish these from each other. Studying localization properties of the bulk states of the Fibonacci chain thus requires not only keeping track of the length scales over which states localize, but also their local environments. Put another way, the IPR takes only into account the square amplitude of individual eigenstates, but also how the eigenstates' phases interact with each other is important. Other tools used to describe localization in a quasicrystal, such as the fractal dimension of the eigenstates [50, 69], show similar restrictions as they are based on generalizations of the IPR.

IV. QUANTUM METRIC

To improve the characterization of localization in quasicrystals, especially the properties for bulk states, which are the vast majority of states, we introduce the quantum metric of the Fibonacci chain. In particular, it is important to better capture the multifractality of the bulk states of the Fibonacci chain [35, 50] than *e.g.* the IPR. Their multifractality in turn influences, or even completely dictates, emergent physical properties [13, 14, 19, 22]. As we will now show, the quantum metric provides a new perspective by much more precisely quantifying the localization properties of especially the bulk eigenstates.

The quantum metric is the real part of the quantum geometric tensor [52], an observable of wave function geometry in the Hilbert space. It measures the volume of the Hilbert space spanned by a given band, or other set of states [52]. In crystalline systems, since the momentum k is a proper quantum number, the quantum metric is usually expressed using derivatives of the wave function

$$\Omega = \frac{1}{2\pi} \int dk \text{Tr} [\partial_k P(k)(1 - P(k))\partial_k P(k)], \quad (11)$$

where $P(k)$ is the projector on the set of occupied bands at momentum k . However, due to the absence of translational

invariance in the Fibonacci chain, the eigenstates cannot be labeled by momentum. We thus need an equivalent formulation in position space. Such a formulation has already been introduced for 2D systems [53, 54]. Here, we extend this formulation to 1D quasicrystals, to be able to apply it to the Fibonacci chain:

$$\Omega = \frac{1}{2\pi N} \int_0^{2\pi} d\phi \text{Tr} \left[P^{(\phi)} x Q^{(\phi)} x P^{(\phi)} \right], \quad (12)$$

where $P^{(\phi)}$ is the projector on the occupied states of the phason mode ϕ , $Q^{(\phi)} = 1 - P^{(\phi)}$, and x is the position operator, while N is the number of sites in the chain. To be able to define the position operator x , the chain needs to have OBCs. Since we are interested in the properties of bulk states, and thus want to avoid that they depend on the chain termination, we use the phason-averaged quantum metric in Eq. (12).

Equation (12) gives the quantum metric a simple interpretation. It measures the second moment of the electron distribution in position space, *i.e.* the spatial extension of the maximally localized Wannier orbitals [53], for a given set of states. Indeed,

$$\text{Tr} [PxQxP] = \text{Tr} [Px^2P] - \text{Tr} [PxPxP] \quad (13)$$

$$= \langle x^2 \rangle - \langle x \rangle^2, \quad (14)$$

where $\langle \cdot \rangle$ is the expectation value over the set of occupied states. Thus, the quantum metric directly encodes the distance between the sites on which the eigenstates are localized [54]. This is in distinct contrast to traditional measures of localization, such as the IPR. Also, it can be seen from Eq. (12) that the quantum metric is non-zero when occupied and unoccupied states lie on the same sites, ensuring that $P^{(\phi)} x Q^{(\phi)} \neq 0$. Thus, setting zero energy to one of the energy gaps, the edge states at positive and negative energies each live at different ends of the chain, resulting in negligible contribution to the quantum metric. As a consequence, the quantum metric must be much more sensitive to the detailed structure of the bulk eigenstates in the Fibonacci chain than the IPR, which we explicitly demonstrate in the following.

In Fig. 3 we quantitatively compare the IPR and the quantum metric as functions of the gap label. We first point out a caveat that the quantum metric is defined for OBCs, while the IPR is better described using PBCs for at least trying to properly analyzing the bulk states. Still, we can make a meaningful comparison between the two cases by noting that for OBCs, the presence of the edge states reduces the number of bulk states and gaps, such that the approximant F_{13} under OBCs has the same gap structure as F_{12} under PBCs. Thus, we get the most meaningful comparison by computing the IPR for the approximant F_{12} and the quantum metric for the approximant F_{13} (or similar for other approximants). See Appendix A for further details about the differences between OBC and PBC. Figure 3(a) plots the IPR of the states lying at the edge of the conduction and valence bands, immediately below and above each gap. Compared to the data shown in Fig. 2(b), the PBCs allow us to get rid of the edge states, which produce the high peaks in Fig. 2(b). As seen, the IPR of the bulk states simply exhibits plateaus for long swaths of gap labels, thus

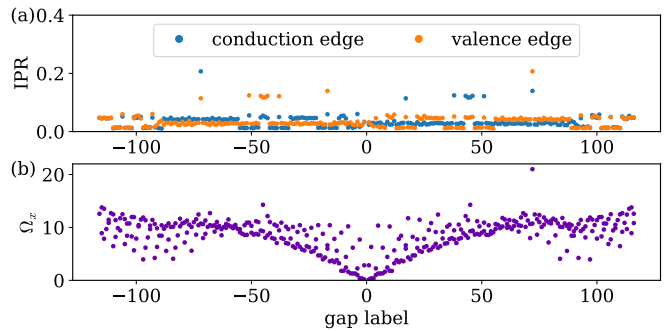


Figure 3. (a) IPR of the bulk states in the 233-site-long approximant F_{12} under PBCs, with modulation strength $\delta = 0.5$. For each gap, we plot the IPRs of the states at the valence and conduction band edges. (b) Quantum metric of the 377-site approximant F_{13} , averaged over phason modes, as a function of gap labels. Under OBCs, due to the presence of edge states, this chain has only 233 bulk gaps. The quantum metric smoothly increases with gap label as higher gap labels separate bands sharing a larger similar environment.

being unable to resolve any fine structure of the localization landscape. Hence the IPR cannot be used to evaluate the localization of the bulk states.

In Fig. 3(b), the quantum metric of each energy gap is obtained by considering all states below the gap as occupied. Despite some fluctuations, the quantum metric displays a clear structure, with both a smooth increase as a function of gap label and clear bounds. The upper bound is independent of gap label and in fact stems from the finite size of the approximant. Indeed, the spread of the states, and thus the quantum metric, can never be larger than the squared length of the chain, which thus sets the upper bound. Longer approximants would be necessary to resolve the difference between such extended bulk states and true Bloch waves with infinite quantum metric. A lower bound is also clearly present and, importantly, smoothly increases as a function of gap label, creating the overall structure. Indeed, this is not just a strict lower bound but most gaps have a quantum metric that even closely tracks this bound. This means that as the gaps get narrower (larger gap labels), the electrons consistently hybridize into states stretching over ever larger scales. However, for absolute gap labels larger than around 60 in Fig. 3(b), the quantum metric saturates and decreases in some gaps, which we attribute to finite size effects. This is consistent with the picture of requiring larger and larger local neighborhoods to resolve states around ever narrower gaps, also resulting in edge states penetrating far into the bulk. Thus we already establish here that the quantum metric is a distinguishable, yet simply accessible, observable and probe of spatial properties of the eigenstates in quasicrystals. Moreover, our results demonstrate that, by setting the filling fraction of the electronic states, which sets the Fermi level in a specific gap, it is possible to tune the localization length of the eigenstates to range from completely trivial localization to a delocalization over the full length of the chain. Further tunability is also offered by changing the modulation strength of the chain.

V. RENORMALIZATION SCHEME AND QUANTUM METRIC

In order to understand the strong relation between the quantum metric and the gap label, and thus understand why the quantum metric is a natural measure of localization in quasicrystals, it is useful to discuss the renormalization group scheme that relates different approximants of the Fibonacci chain and their gap structure. Due to the scale-invariance properties of the Fibonacci chain, its eigenstates inherit a cascade of symmetries at all scales [33, 66, 70]. We here illustrate these symmetries using a real-space renormalization-group approach. Figure 4 summarizes the band structures of the first few approximants of the Fibonacci chain under PBCs, with the corresponding local symmetry eigenvalues, with H_n being the set of symmetry eigenvalues of the bands obtained from the approximant F_n . The shortest approximants F_0 and F_1 have just one type of bonds, and thus form only one band. All sites are thus local symmetry centers of the chain and the band can be said to have an atomic symmetry, which we denote by "o". The next approximant F_2 corresponds to the SSH polyacetylen chain [71]. In this approximant, the local symmetry centers lie on the bond, and the spectrum thus decomposes into two molecular bands lying on a dimer, one symmetric (+) and one antisymmetric (-) with respect to the bond center. The first non-trivial approximant F_3 (under PBC) hosts two kinds of local environments: atomic sites ($t_L \cdot t_L$ chain segments), and molecular dimers ($t_L \cdot t_S \cdot t_L$). Thus, its spectrum decomposes into an atomic band (o) localized on atomic sites, flanked in energy by the molecular symmetric (+) and antisymmetric (-) bands occupying dimers.

It is now interesting to note that longer approximants retain the main three-band structure found in the first four approximants. This directly stems from the scale-invariance of the Fibonacci chain and indicates that the eigenstates of all approximants can be characterized by a local symmetry eigenvalue: +, - or o. As we construct longer approximants, the three main bands also split into sub-bands, that can be associated to symmetries emerging at longer scales. For example, F_5 hosts the same three types of local environments as F_3 , but we can further distinguish sites based on their larger environment: dimers can be either grouped as pairs when they are separated by a single long bond ($t_L t_L \cdot t_S \cdot t_L \cdot t_S \cdot t_L t_L$) or isolated if they are only surrounded by long bonds ($t_L t_L \cdot t_S \cdot t_L t_L$); while atomic sites all get grouped as pairs separated by a dimer ($t_L \cdot t_L t_S t_L \cdot t_L$). As a consequence, the atomic band (o) inherits long-range symmetries from F_2 (purple rectangle in Fig. 4) and thus splits into atomic symmetric (o+) and atomic antisymmetric (o-) bands. Similarly, the molecular bands (\pm) split into three sub-bands, inheriting long-range symmetries from F_3 (green rectangles in Fig. 4). They form two molecular-atomic (+o, -o) and four molecular-molecular (+++, ++-, -+-, ---) bands. With the energy splitting being lower for the atomic bands, this together results in the structure shown for F_5 in Fig. 4.

Generalizing the scheme displayed in Fig. 4 to ever larger approximants, their sub-band structure can be obtained from shorter approximants after performing a step of the renormal-

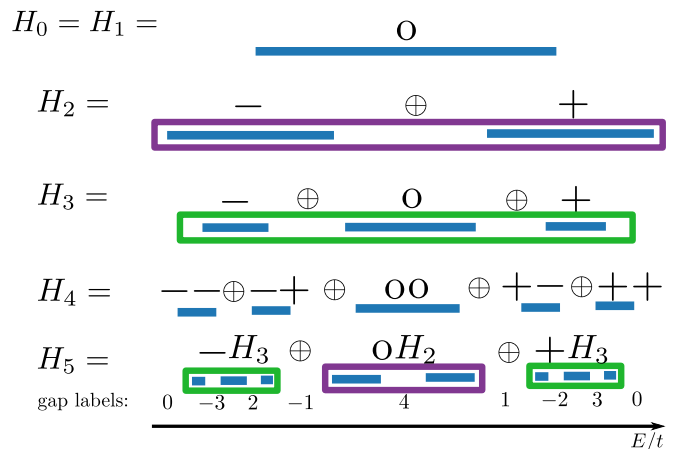


Figure 4. Schematic band structure of the six smallest Fibonacci approximants along with their symmetry eigenvalues. Blue lines are illustrations of the band structure of each approximant, but with length not to scale. To each band corresponds a set of symmetry eigenvalues representing atomic (o), molecular symmetric (+) and molecular antisymmetric (-) characters, with H_n being the set of symmetry eigenvalues of the bands obtained from the approximant F_n . The symmetry eigenvalues of different (larger) bands are separated by \oplus . The two trivial approximants F_0 and F_1 share the same spectrum. Then, F_2 is the SSH chain, with two bands. The spectra of the following approximants are obtained from Eq. (17). Gap labels of F_5 are also shown.

ization scheme. Indeed, H_n for any n can be obtained from the recursion relation [50, 66],

$$H_0 = H_1 = o, \quad (15)$$

$$H_2 = - \oplus +, \quad (16)$$

$$H_n = -H_{n-2} \oplus oH_{n-3} \oplus +H_{n-2}, \quad (17)$$

where the symmetry labels of each band (o, \pm) are ordered by smaller local atomic environment on the left to larger ones on the right. Overall, this structure also gives the ordering of the band in energy. Each band of every approximant can therefore be labeled by a set of symmetry eigenvalues at different scales. The gap labels in turn keep track of this hierarchy of symmetry, since the smallest absolute labels separate bands with different symmetries at local scales, whereas larger gap labels, both positive and negative, only appear in long approximants, where long-range symmetries have to be taken into account. For example, in Fig. 4 the gaps of H_5 with labels ± 1 separate atomic from molecular bands at the nearest neighbor scale, while gaps ± 2 , ± 3 and 4 separate bands with the same nearest neighbor symmetry, but different second-order nearest neighbor symmetry labels.

The fact that the Fibonacci bands can be classified based on the local symmetries of the eigenstates they contain makes the quantum metric a very natural probe of their localization. Indeed, the quantum metric is maximally sensitive to having symmetric and antisymmetric states sharing the same symmetry center being either occupied or empty, and it is then proportional to the square of the spatial extent of such dimerized states. To illustrate explicitly how this is manifested in the

Fibonacci chain, let us consider two groups of sites related by a spatial mirror symmetry. As explained in Sec. II, such sites can be labeled by opposite conumbers $n = (n_1, n_2, \dots, n_i)$ and $-n = (-n_i, \dots, -n_2, -n_1)$. The spectrum of the Fibonacci chain then contains two states of opposite energy that are made of symmetric and antisymmetric superpositions of those groups of sites, which we may denote $|\pm\rangle = (|n\rangle \pm |-n\rangle)/\sqrt{2}$. Following Eq. (12), this pair of states contributes to the quantum metric at all fillings where only one of them is occupied. Assuming, with no loss of generality, that $P|+\rangle = |+\rangle$ and $Q|-\rangle = |-\rangle$, then the following term appears in the sum of the quantum metric in Eq. (12)

$$\begin{aligned} \langle +|x|-\rangle \langle -|x|+\rangle &= |\langle +|x|-\rangle|^2 \\ &= (\langle n|x|n\rangle - \langle -n|x| -n\rangle)^2 = (x_n - x_{-n})^2. \end{aligned} \quad (18)$$

Thus the quantum metric measures the spread, or extent, of the dimerized state between these two groups of sites related by a mirror symmetry. As shown in Fig. 4, each gap in the spectrum opens due to the hybridization of two similar groups of sites into symmetric and antisymmetric superpositions. Then Eq. (18) gives that the quantum metric calculated in that gap includes the measure of the square distance between these two groups of sites. Thus, the smooth increase of the quantum metric as a function of gap labels shown in Fig. 3(b) is directly related to the fact that the gaps appearing deeper in the spectrum are associated to larger groups of sites, associated larger spatial separation in Eq. (18) compared to smaller (absolute valued) gap labels. This establishes the quantum metric as a natural measure of localization and spatial structure of the eigenstates of quasicrystals.

VI. MINIMAL BOUND FOR THE QUANTUM METRIC

The quantum metric in Fig. 3(b) seems to imply even the possibility of a firm lower bound to the quantum metric as a function of gap label. This is reminiscent of the inequality relating the quantum metric to the Chern number C in 2D Chern insulators, $\Omega > \frac{|C|}{\pi}$ [55]. However, this relation cannot apply here since the Fibonacci chain is just 1D [37], whereas at least two dimensions are required to define the Berry curvature and the Chern number [72]. We are still able to proceed by noting that the Fibonacci chain can be mapped on a 2D parameter space by using not just the position, but also the phason parameter, or angle, as coordinates [36–38]. The Hamiltonian of the chain then reads

$$\mathcal{H} = \int d\phi \sum_n t_n(\phi) c_n^\dagger(\phi) c_{n+1}(\phi) + \text{H.c.}, \quad (19)$$

where ϕ labels the different phason modes of the considered approximant. The difference with Eq. (9) is thus that ϕ is now considered as a degree of freedom of the system, as indicated by the dependence of the operators $c_n^{(\dagger)}$ and nearest neighbor hopping $t_n(\phi)$ on both n and ϕ . Here $t_n(\phi)$ is given by Eq. (10). As explained in Sec. II, the phason parameter is

a momentum-like degree of freedom and therefore an extension to a synthetic second dimension spanned by the phason angle results in a mixed real-space and (synthetic) momentum Hamiltonian.

Since we are utilizing the quantum metric to measure the degree of localization of the electronic states in position space, it is in some situations also useful to introduce a complementary position-space picture corresponding to the phasonic degree of freedom. We can accomplish this by decomposing Eq. (10) into a Fourier series

$$t_n(\phi) = \sum_{l=-\infty}^{l=+\infty} \tilde{t}_n^l e^{-il\phi}, \quad (20)$$

where

$$\tilde{t}_n^0 = \frac{t_L + t_S}{2} \left(1 + \delta \left(2 \frac{q}{p+q} - 1 \right) \right), \quad (21)$$

and for $l \neq 0$

$$\tilde{t}_n^l = \frac{t_S - t_L}{2} \frac{2}{\pi l} \sin \left(\frac{\pi l q}{p+q} \right) e^{2i\pi l(n+1) \frac{q}{p+q}}. \quad (22)$$

In Eq. (20), the term \tilde{t}_n^l corresponds to a hopping from site (n, m) to site $(n+1, m+l)$, where m , hereafter referred to as the conjugate position, labels the 'position' along the phasonic direction, *i.e.* the position degree of freedom conjugate to the phason parameter. The sharp switch from t_L to t_S and vice-versa as a function of ϕ in Eq. (10) results in a slow decay of the harmonics as a function of l , $|\tilde{t}_n^l| \underset{l \rightarrow \infty}{\sim} \frac{1}{l}$. These high harmonics correspond to long-range hoppings along the conjugate position axis.

The Hamiltonian in Eq. (19) now describes a 2D system, mixing a position degree of freedom x and a momentum-like one ϕ . As such, it can be characterized by a Chern number, although the computation of a Chern number usually relies on the Berry curvature in momentum space only [73]. However, Bianco *et al.* [74] have introduced a new formulation for the Berry curvature, fully expressed in terms of position degrees of freedom. Here, we merge these two diametrical opposite approaches into a new formulation of the Chern number that mixes position space along one dimension with momentum space along the other:

$$\begin{aligned} C = \frac{1}{2i\pi N} \int_0^{2\pi} d\phi \text{Tr}_{\text{bulk}} [&P^{(\phi)} x Q^{(\phi)} \partial_\phi P^{(\phi)} \\ &- \partial_\phi P^{(\phi)} Q^{(\phi)} x P^{(\phi)}], \end{aligned} \quad (23)$$

where N is the number of sites in the chain, and $P^{(\phi)}, Q^{(\phi)}$, are projectors on the occupied and unoccupied states, respectively of the phason mode ϕ . We set the bulk sites over which the trace is computed when using OBCs as (arbitrarily) the central third of the chain to capture bulk properties. Similarly, we have to formulate a new two-component quantum metric incorporating both position space and phason degrees of freedom,

$$\Omega = \Omega_x + \Omega_\phi, \quad (24)$$

which read

$$\Omega_x = \frac{1}{2\pi} \int_0^{2\pi} d\phi \text{Tr}[P^{(\phi)} x Q^{(\phi)} x], \quad (25)$$

and

$$\Omega_\phi = \frac{1}{2\pi} \int_0^{2\pi} d\phi \text{Tr} \left[\partial_\phi P^{(\phi)} Q^{(\phi)} \partial_\phi P^{(\phi)} \right]. \quad (26)$$

Here the positional component Ω_x of the 2D quantum metric Ω in Eq. (24) is the exact same as the Fibonacci chain 1D quantum metric in Eq. (12). The phasonic component is however new and involves derivatives with respect to the phason parameter, as expected for a quantum metric computed in momentum space, see Eq. (11). Note that the quantum metric does not mix the degrees of freedom as the Chern number, but instead consists of two additive individual contributions. Also note that, contrary to the Chern number, the components of the quantum metric can be traced over the full system also when using OBCs. This is because the edge sites do not bring a specific contribution to the quantum metric, whereas bulk and edge sites have opposite contributions to the Chern number in Eq. (23), with only the bulk sites being quantized to the Chern number [74].

We further note that Eqs. (23) and (24) are defined for a continuous phason parameter, whereas the phason modes in fact remain discrete due to the sign function in Eq. (10). In principle, the derivatives with respect to ϕ are thus ill-defined for the Fibonacci chain, as the hoppings suddenly switch between t_L and t_S for two different phason modes. This results in Ω_ϕ diverging in the thermodynamic limit. Remarkably, the Chern number (23) in a given gap does not diverge in the thermodynamic limit, due to the fact that it contains only one ϕ -derivative of a sign function, which can be described in terms of Dirac-delta distributions and are in turn integrable. The divergence of Ω_ϕ can also be seen from the position space picture as Eq. (20) effectively allows infinite-range hoppings along the phasonic direction, thus resulting in fully delocalized electronic states, with accompanied diverging quantum metric. To avoid this divergence and keep a smooth variation of the Hamiltonian as a function of ϕ , we introduce a cutoff $|l| < L$ in the series in Eq. (20). In the phasonic space, this cutoff smoothens the change between two phason modes while, in the conjugate position space picture, hoppings with range greater than L become forbidden. In principle, this cutoff can strongly influence both the spectrum and the eigenstates of the system. For example, gaps with label $|\nu| > L$ do not open in the smoothed version of the Fibonacci chain. A similar effect is also known to appear in 2D Chern insulators [75]: long-range hoppings are necessary to obtain high-Chern-number insulators. Thus, in order to keep the gap structure of the spectrum of the chain, we choose the cutoff L to be the size of the approximant N , so that it does not close any gaps.

Having defined a 2D Chern number in Eq. (23) and 2D quantum metric in Eq. (24) for the 1D Fibonacci chain, we plot in Fig. 5 both of these quantities computed in the gaps of the approximant F_9 , with a cutoff $L = N = 55$ for two different chain modulations δ . In order to limit finite-size

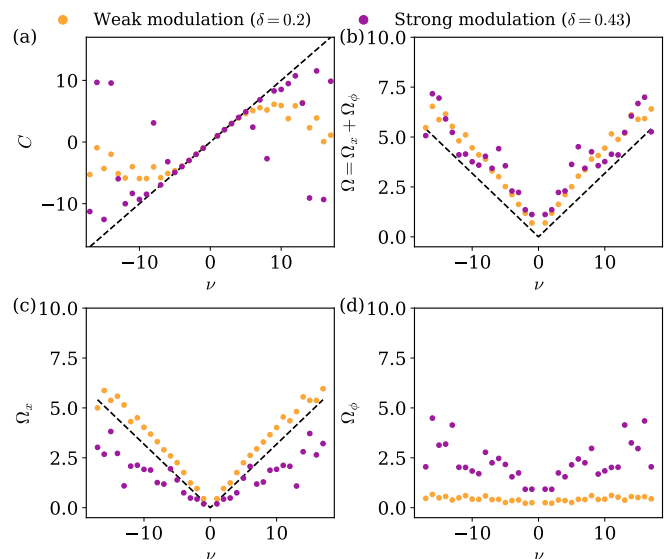


Figure 5. Chern number C and quantum metric $\Omega = \Omega_x + \Omega_\phi$ as a function of the gap label ν with two colors corresponding to different modulation strengths $\delta = 0.2$, or $\delta = 0.43$, using the 55-site approximant F_9 and OBCs. In order to limit finite-size effects, we consider a chain made of three concatenations of F_9 and use a cutoff $L = N = 55$ for the phasonic components. (a) Chern number C , computed according to Eq. (23). Black dashed line indicates $C = \nu$. (b) Full quantum metric Ω , according to Eq. (24). Black dashed line indicates $\Omega = \frac{|C|}{\pi}$. (c) Positional component Ω_x of the quantum metric, according to Eq. (25). Black dashed line indicates $\Omega_x = \frac{|C|}{\pi}$. (d) Phasonic component Ω_ϕ of the quantum metric, according to Eq. (26).

effects, we consider a chain made of three concatenations of F_9 with OBCs. In the largest gaps, the Chern number in Fig. 5(a) converges to the gap label $C = \nu$ (dashed line). This result confirms an earlier derived relationship between gap label and Chern number in 2D when both position and phason parameters are considered as degrees of freedom [36–38]. For small gaps, the result of Eq. (23) deviates from this quantization. We attribute this to finite size effects since, when the gaps get narrower, the edge states penetrate deeper in the bulk thus mitigating the bulk quantization necessary for the Chern number. This is also the reason why a chain with strong modulation displays better quantization than a weakly modulated chain.

In Figs. 5(b-d) we plot both the total quantum metric (b) and its positional (c) and phasonic (d) components and compare these to the Chern number. In Fig. 5(b) we immediately see how the full quantum metric Ω is lower bounded by the gap label and Chern number C (dashed line). Thanks to the above derived analogy to a 2D Chern insulator, we can even analytically derive, following Ref. [55], an inequality relating the full quantum metric Ω and the Chern number C as

$$\Omega > \frac{|C|}{\pi}, \quad (27)$$

which for the quasicrystal thus applies to the full quantum

metric $\Omega = \Omega_x + \Omega_\phi$.

Having derived a lower bound of the full quantum metric Ω , it is interesting to also focus on the relative weight of the two components of the quantum metric, Ω_ϕ and Ω_x , as a function of the modulation strength δ . For non-zero but weak modulations $\delta \ll 1$, the phasonic part of the quantum metric remains very small $\Omega_\phi \ll \Omega_x$, compare Figs. 5(c,d). In this regime, the full quantum metric Ω thus coincides with the positional quantum metric Ω_x of the 1D Fibonacci chain, $\Omega_x \sim \Omega$. Specifically, Eq. (27) can be rewritten as $\Omega_x \underset{\delta \ll 1}{>} \frac{|C|}{\pi}$, which establishes that the localization properties, as measured by the quantum metric, must at least be linearly growing with the gap label. Moreover, since the positional quantum metric Ω_x is not just bounded from below by the gap label, but also closely tracks it in this low modulation regime as seen in both Fig. 3(b) and Fig. 5(c), we conclude that the eigenstates of the Fibonacci chain directly inherit their localization properties from those of a 2D Chern insulator. This establishes a direct link between the spatial localization, characterized by the quantum metric, and the energy spectrum, as quantified by the gap label, in weakly modulated quasicrystals.

For strong modulations, $\delta \sim 1$, the phasonic part becomes more dominant in the full quantum metric. The position component Ω_x still increases with gap label, but the strict inequality with the gap label does not hold for only Ω_x . However, we note that we cannot really deduce useful information for the 1D Fibonacci from the phasonic part alone as it is strongly influenced by the cutoff L . In fact, in the strong-modulation regime, the eigenstates delocalize along the phasonic dimension, resulting in $\Omega_\phi \propto L^2$.

VII. CONCLUDING REMARKS

In this work, we use the quantum metric to study the localization properties of the eigenstates in a quasicrystal, focusing on the 1D Fibonacci chain. The quantum metric probes the real-space spread of the electronic states. In contrast to the IPR, it can thus efficiently discriminate states occupying the same number of sites, but with different separation in space, while still being an easily accessible observable. As we establish, the quantum metric even captures the importance of the many local symmetry centers present within the quasicrystal. Since such local symmetry centers are concatenated throughout the chain in a scale-invariant fashion, the quantum metric is in many ways an optimal and natural probe of locality on quasicrystals. With the quantum metric being numerically easily accessible and with experimental probes of it being rapidly uncovered [62], the quantum metric thus offers great promise for understanding the physics of quasicrystals, both theoretically and experimentally.

Our results also demonstrate that the quantum metric is strongly connected to the many energy gaps present in quasicrystals. These gaps occur due to the hybridization between local symmetry-centered states, and thus the quantum metric is a natural quantity to connect structure with energy. In fact, we find numerically that the quantum metric is closely track-

ing the gap label associated with each gap. By introducing an additional phasonic component to the quantum metric, we are even able to analytically establish that the full quantum metric, the sum of the spatial and phasonic parts, is lower bounded by the Chern number of a 2D Chern insulator, also created by appending the spatial dimension with the same phasonic component. Since the same Chern number is already known to generate the gap labels [36], this put an analytical lower bound on the full quantum metric to the gap labels. Thus our work provides a direct link between spatial localization in a quasicrystal and its energy spectrum. This link is even formally exact in the limit of small quasicrystalline modulations, where we can ignore the phasonic part of the quantum metric. The bound also directly shows that the localization properties of the bulk eigenstates in the 1D Fibonacci chain can be inferred from that of a 2D crystalline system. Taken together, the Chern number and the quantum metric form the quantum geometric tensor [52], which thus provides a comprehensive tool to understand many distinctive aspects of the quasicrystals.

The relation between properties of a 1D quasicrystal and a 2D crystal fundamentally stems from the fact that the 1D Fibonacci chain can be built by projecting a 2D square lattice on a line, as emphasized by the cut-and-project method described in Sec. II. The cut-and-project method is in fact a general method to obtain quasicrystals, in any dimension [76–78]. Thus, the approach we develop here to understand localization can be adapted to other quasicrystals, whose spatial localization properties, expressed through the full quantum metric, are then also inherited from higher-dimensional crystals, independent of them being topological or not. This is reminiscent of the already establish relation between the properties of quasicrystals and their higher-dimensional parent crystals in terms of their topological properties [6], while here we establish it also for the localization properties.

Beyond the quest for understanding and characterizing of the peculiar localization properties of quasicrystals, our work also emphasizes the quantum metric as an indispensable tool to quantify localization in scale-invariant systems and relate it to physical observables. Indeed, the quantum metric incorporates the notion of distance in real space, which is absent in many other tools currently used to study localization, such as the IPR. Moreover, the quantum metric can be directly related to easily accessible observables, such as conductivity [79] and optical responses [80], making it an experimentally accessible probe. In the presence of electronic correlations, it has also been shown to be related to the superfluid weight in flat-bands superconductors [55, 56, 81] and the occurrence of fractional quantum Hall effect in Chern insulators [57–59]. This is an especially intriguing future direction, given the growing interest in superconducting quasicrystals [10–23].

Acknowledgements.— We thank A. Bhattacharya, and A. Jagannathan for interesting and fruitful discussions related to this work. We acknowledge funding from the Swedish Research Council (Vetenskapsrådet Grant No. 2022-03963) and the European Union through the European Research Council (ERC) under the European Union’s Horizon 2020 research and innovation programme (ERC-2022-CoG, Grant Agreement No. 101087096). Views and opinions expressed are

however those of the authors only and do not necessarily reflect those of the European Union or the European Research Council Executive Agency. Our calculations were performed

using the Python package Kwant [82] and our plots using matplotlib [83]. The code used for the numerical calculations and the data shown in the manuscript are available at Ref. [84].

-
- [1] D. Shechtman, I. Blech, D. Gratias, and J. W. Cahn, *Phys. Rev. Lett.* **53**, 1951 (1984).
- [2] N. Macé, A. Jagannathan, P. Kalugin, R. Mosseri, and F. Piéchon, *Phys. Rev. B* **96**, 045138 (2017).
- [3] Y. E. Kraus, Y. Lahini, Z. Ringel, M. Verbin, and O. Zilberberg, *Phys. Rev. Lett.* **109**, 106402 (2012).
- [4] D. Varjas, A. Lau, K. Pöyhönen, A. R. Akhmerov, D. I. Pikulin, and I. C. Fulga, *Phys. Rev. Lett.* **123**, 196401 (2019).
- [5] G. Rai, H. Schlömer, C. Matsumura, S. Haas, and A. Jagannathan, *Phys. Rev. B* **104**, 184202 (2021).
- [6] D. V. Else, S.-J. Huang, A. Prem, and A. Gromov, *Phys. Rev. X* **11**, 041051 (2021).
- [7] J. Fan and H. Huang, *Front. Phys.* **17**, 13203 (2022).
- [8] N. Macé, N. Laflorencie, and F. Alet, *SciPost Phys.* **6**, 050 (2019).
- [9] C. Chiaracane, F. Pietracaprina, A. Purkayastha, and J. Goold, *Phys. Rev. B* **103**, 184205 (2021).
- [10] S. Sakai, N. Takemori, A. Koga, and R. Arita, *Phys. Rev. B* **95**, 024509 (2017).
- [11] K. Kamiya, T. Takeuchi, N. Kabeya, N. Wada, T. Ishimasa, A. Ochiai, K. Deguchi, K. Imura, and N. K. Sato, *Nat. Commun.* **9**, 154 (2018).
- [12] R. N. Araújo and E. C. Andrade, *Phys. Rev. B* **100**, 014510 (2019).
- [13] X. Zhang and M. S. Foster, *Phys. Rev. B* **106**, L180503 (2022).
- [14] Y. Wang, G. Rai, C. Matsumura, A. Jagannathan, and S. Haas, *Phys. Rev. B* **109**, 214507 (2024).
- [15] N. S. Ticea, J. May-Mann, J. Xiao, E. Berg, and T. Devakul, *Phys. Rev. B* **110**, L060501 (2024).
- [16] Y. Tokumoto, K. Hamano, S. Nakagawa, Y. Kamimura, S. Suzuki, R. Tamura, and K. Edagawa, *Nature Communications* **15**, 1529 (2024).
- [17] G. Rai, S. Haas, and A. Jagannathan, *Phys. Rev. B* **100**, 165121 (2019).
- [18] G. Rai, S. Haas, and A. Jagannathan, *Phys. Rev. B* **102**, 134211 (2020).
- [19] A. Sandberg, O. A. Awoga, A. M. Black-Schaffer, and P. Holm-vall, *Phys. Rev. B* **110**, 104513 (2024).
- [20] I. C. Fulga, D. I. Pikulin, and T. A. Loring, *Phys. Rev. Lett.* **116**, 257002 (2016).
- [21] R. Ghadimi, T. Sugimoto, K. Tanaka, and T. Tohyama, *Phys. Rev. B* **104**, 144511 (2021).
- [22] A. Kobiałka, O. A. Awoga, M. Leijnse, T. Domański, P. Holm-vall, and A. M. Black-Schaffer, *Phys. Rev. B* **110**, 134508 (2024).
- [23] M. Hori, T. Sugimoto, T. Tohyama, and K. Tanaka, *Phys. Rev. B* **110**, 144512 (2024).
- [24] R. Tamura, T. Abe, S. Yoshida, Y. Shimosaki, S. Suzuki, A. Ishikawa, F. Labib, M. Avdeev, K. Kinjo, K. Nawa, and T. J. Sato, *Nat. Phys.* **10.1038/s41567-025-02858-0** (2025).
- [25] S. M. Lubin, W. Zhou, A. J. Hryn, M. D. Huntington, and T. W. Odom, *Nano Lett.* **12**, 4948 (2012).
- [26] S. J. Ahn, P. Moon, T.-H. Kim, H.-W. Kim, H.-C. Shin, E. H. Kim, H. W. Cha, S.-J. Kahng, P. Kim, M. Koshino, Y.-W. Son, C.-W. Yang, and J. R. Ahn, *Science* **361**, 782 (2018).
- [27] R. Mahmood, A. V. Ramirez, and A. C. Hillier, *ACS Appl. Nano Mater.* **4**, 8851 (2021).
- [28] A. Uri, S. C. de la Barrera, M. T. Randeria, D. Rodan-Legrain, T. Devakul, P. J. D. Crowley, N. Paul, K. Watanabe, T. Taniguchi, R. Lifshitz, L. Fu, R. C. Ashoori, and P. Jarillo-Herrero, *Nature* **620**, 762 (2023).
- [29] A. Jagannathan, *Rev. Mod. Phys.* **93**, 045001 (2021).
- [30] M. Kohmoto, L. P. Kadanoff, and C. Tang, *Phys. Rev. Lett.* **50**, 1870 (1983).
- [31] S. Ostlund, R. Pandit, D. Rand, H. J. Schellnhuber, and E. D. Siggia, *Phys. Rev. Lett.* **50**, 1873 (1983).
- [32] Sire, Clément and Mosseri, Rémy, *J. Phys. France* **50**, 3447 (1989).
- [33] F. Piéchon, M. Benakli, and A. Jagannathan, *Phys. Rev. Lett.* **74**, 5248 (1995).
- [34] A. Moustaj, M. Röntgen, C. V. Morfonios, P. Schmelcher, and C. Morais Smith, *New Journal of Physics* **25**, 093019 (2023).
- [35] M. Reisner, Y. Tahmi, F. Piéchon, U. Kuhl, and F. Mortessagne, *Phys. Rev. B* **108**, 064210 (2023).
- [36] Y. E. Kraus and O. Zilberberg, *Phys. Rev. Lett.* **109**, 116404 (2012).
- [37] K. A. Madsen, E. J. Bergholtz, and P. W. Brouwer, *Phys. Rev. B* **88**, 125118 (2013).
- [38] A. Jagannathan, *Missing link between the 2D Quantum Hall problem and 1D quasicrystals* (2025), arXiv:2506.01122 [cond-mat.str-el].
- [39] L. Dal Negro, C. J. Oton, Z. Gaburro, L. Pavesi, P. Johnson, A. Lagendijk, R. Righini, M. Colocci, and D. S. Wiersma, *Phys. Rev. Lett.* **90**, 055501 (2003).
- [40] W. Steurer and D. Sutter-Widmer, *J. Phys. D: Appl. Phys.* **40**, R229 (2007).
- [41] M. Verbin, O. Zilberberg, Y. E. Kraus, Y. Lahini, and Y. Silberberg, *Phys. Rev. Lett.* **110**, 076403 (2013).
- [42] D. Tanese, E. Gurevich, F. Baboux, T. Jacqmin, A. Lemaître, E. Galopin, I. Sagnes, A. Amo, J. Bloch, and E. Akkermans, *Phys. Rev. Lett.* **112**, 146404 (2014).
- [43] M. Verbin, O. Zilberberg, Y. Lahini, Y. E. Kraus, and Y. Silberberg, *Phys. Rev. B* **91**, 064201 (2015).
- [44] F. Baboux, E. Levy, A. Lemaître, C. Gómez, E. Galopin, L. Le Gratiet, I. Sagnes, A. Amo, J. Bloch, and E. Akkermans, *Phys. Rev. B* **95**, 161114(R) (2017).
- [45] F. Lisiecki, J. Rychły, P. Kuświk, H. Głowiński, J. W. Kłos, F. Groß, N. Träger, I. Bykova, M. Weigand, M. Zelent, E. J. Goering, G. Schütz, M. Krawczyk, F. Stobiecki, J. Dubowik, and J. Gräfe, *Phys. Rev. Appl.* **11**, 054061 (2019).
- [46] V. Goblot, A. Štrkalj, N. Pernet, J. L. Lado, C. Dorow, A. Lemaître, L. Le Gratiet, A. Harouri, I. Sagnes, S. Ravets, A. Amo, J. Bloch, and O. Zilberberg, *Nat. Phys.* **16**, 832 (2020).
- [47] S. Franca, T. Seidemann, F. Hassler, J. van den Brink, and I. C. Fulga, *Phys. Rev. B* **109**, L241103 (2024).
- [48] H. Yao, A. Khoudli, L. Bresque, and L. Sanchez-Palencia, *Phys. Rev. Lett.* **123**, 070405 (2019).
- [49] Y. Lahini, R. Pugatch, F. Pozzi, M. Sorel, R. Morandotti, N. Davidson, and Y. Silberberg, *Phys. Rev. Lett.* **103**, 013901 (2009).
- [50] N. Macé, A. Jagannathan, and F. Piéchon, *Phys. Rev. B* **93**, 205153 (2016).
- [51] A. Ahmed, A. Ramachandran, I. M. Khaymovich, and

- A. Sharma, *Phys. Rev. B* **106**, 205119 (2022).
- [52] J. Provost and G. Vallee, *Communications in Mathematical Physics* **76**, 289 (1980).
- [53] N. Marzari and D. Vanderbilt, *Phys. Rev. B* **56**, 12847 (1997).
- [54] Q. Marsal and A. M. Black-Schaffer, *Phys. Rev. Lett.* **133**, 026002 (2024).
- [55] S. Peotta and P. Törmä, *Nat. Commun.* **6**, 8944 (2015).
- [56] H. Tian, X. Gao, Y. Zhang, S. Che, T. Xu, P. Cheung, K. Watanabe, T. Taniguchi, M. Randeria, F. Zhang, *et al.*, *Nature* **614**, 440 (2023).
- [57] E. J. BERGHOLTZ and Z. LIU, *International Journal of Modern Physics B* **27**, 1330017 (2013), <https://doi.org/10.1142/S021797921330017X>.
- [58] P. J. Ledwith, G. Tarnopolsky, E. Khalaf, and A. Vishwanath, *Phys. Rev. Res.* **2**, 023237 (2020).
- [59] D. Varjas, A. Abouelkomsan, K. Yang, and E. J. Bergholtz, *SciPost Phys.* **12**, 118 (2022).
- [60] T. Neupert, C. Chamon, and C. Mudry, *Phys. Rev. B* **87**, 245103 (2013).
- [61] M. Kang, S. Kim, Y. Qian, P. M. Neves, L. Ye, J. Jung, D. Puntel, F. Mazzola, S. Fang, C. Jozwiak, A. Bostwick, E. Rotenberg, J. Fuji, I. Vobornik, J.-H. Park, J. G. Checkelsky, B.-J. Yang, and R. Comin, *Nature Physics* **21**, 110 (2025).
- [62] N. Verma, P. J. W. Moll, T. Holder, and R. Queiroz, *Quantum geometry: Revisiting electronic scales in quantum matter* (2025), [arXiv:2504.07173](https://arxiv.org/abs/2504.07173) [cond-mat.mtrl-sci].
- [63] J. Q. You and T. B. Hu, *physica status solidi (b)* **147**, 471 (1988), <https://onlinelibrary.wiley.com/doi/pdf/10.1002/pssb.2221470203>.
- [64] M. Röntgen, C. V. Morfonios, R. Wang, L. Dal Negro, and P. Schmelcher, *Phys. Rev. B* **99**, 214201 (2019).
- [65] T. O. Wehling, S. Yuan, A. I. Lichtenstein, A. K. Geim, and M. I. Katsnelson, *Phys. Rev. Lett.* **105**, 056802 (2010).
- [66] N. Macé, A. Jagannathan, and F. Piéchon, *Journal of Physics: Conference Series* **809**, 012023 (2017).
- [67] A. Moustaj, S. Kempkes, and C. M. Smith, *Phys. Rev. B* **104**, 144201 (2021).
- [68] A. Agarwala and V. B. Shenoy, *Phys. Rev. Lett.* **118**, 236402 (2017).
- [69] S. Thiem and M. Schreiber, *Journal of Physics: Condensed Matter* **25**, 075503 (2013).
- [70] C. Morfonios, P. Schmelcher, P. Kalozoumis, and F. Diakonou, *Nonlinear Dynamics* **78**, 71 (2014).
- [71] W. P. Su, J. R. Schrieffer, and A. J. Heeger, *Phys. Rev. Lett.* **42**, 1698 (1979).
- [72] C.-K. Chiu, J. C. Y. Teo, A. P. Schnyder, and S. Ryu, *Rev. Mod. Phys.* **88**, 035005 (2016).
- [73] M. V. Berry, *Proceedings of the Royal Society of London. A. Mathematical and Physical Sciences* **392**, 45 (1984).
- [74] R. Bianco and R. Resta, *Phys. Rev. B* **84**, 241106 (2011).
- [75] D. Sticlet and F. Piéchon, *Phys. Rev. B* **87**, 115402 (2013).
- [76] Katz, A. and Duneau, M., *J. Phys. France* **47**, 181 (1986).
- [77] M. Duneau and A. Katz, *Phys. Rev. Lett.* **54**, 2688 (1985).
- [78] V. Elser, *Acta Crystallographica Section A* **42**, 36 (1986).
- [79] N. Wang, D. Kaplan, Z. Zhang, T. Holder, N. Cao, A. Wang, X. Zhou, F. Zhou, Z. Jiang, C. Zhang, S. Ru, H. Cai, K. Watanabe, T. Taniguchi, B. Yan, and W. Gao, *Nature* **621**, 487 (2023).
- [80] Z. Li, S. Zhang, T. Tohyama, X. Song, Y. Gu, T. Itaka, H. Su, and H. Zeng, *Science China Physics, Mechanics & Astronomy* **64**, 107211 (2021).
- [81] A. Julku, S. Peotta, T. I. Vanhala, D.-H. Kim, and P. Törmä, *Phys. Rev. Lett.* **117**, 045303 (2016).
- [82] C. W. Groth, M. Wimmer, A. R. Akhmerov, and X. Waintal, *New Journal of Physics* **16**, 063065 (2014).
- [83] J. D. Hunter, *Computing in Science & Engineering* **9**, 90 (2007).
- [84] Q. Marsal, P. Holmval, and A. Black-Schaffer, [10.5281/zenodo.15609220](https://arxiv.org/abs/2504.07173) (2025).

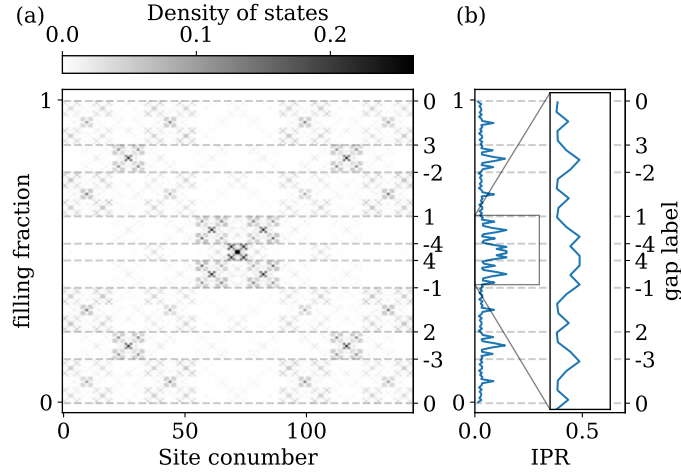


Figure 6. Same figure as Fig. 2, but with PBCs. (a) Local density of states and (b) IPR as a function of filling fraction. By using PBC this is the same data as in Fig. 3(a) but here plotting as a function of filling fraction.

Appendix A: Local density of states and inverse participation ratio under periodic boundary conditions

In Figs. 2(b) and 3(a) in the main text, we plot the IPR of the eigenstates of the Fibonacci chain under different boundary conditions. The OBCs used to plot Fig. 2 allow us to discuss the observation of the edge states with the IPR, and their increased penetration depth for gaps with higher gap labels (*i.e.* with smaller gap sizes). In contrast, in Fig. 3, we discuss the localization of the bulk states and plot both the spatial quantum metric Ω_x and the IPR as functions of the gap label. The formulation of the quantum metric in Eq. (12) is only adapted to OBCs, as it requires us to define the position operator unambiguously, but still, the quantum metric is not strongly affected by the presence of localized edge modes. This is however not true for the IPR, which mainly probe the edge modes, as seen in Fig. 2(b). Therefore, in order to be able to compare the IPR and the quantum metric in Fig. 3, we need to isolate the IPR of the bulk states, which we do by computing the IPR under PBCs in Fig. 3(a). For completeness, we provide here in the Appendix in Fig. 6 the local density of states and the IPR as a function of filling fraction, *i.e.* similarly to Fig. 2, but under PBCs. Compared to Fig. 2(b), the peaks corresponding to the edge states do not show up in Fig. 6(b). With the IPR only depending on the number of sites involved in a given state, we thus find many different states sharing the same IPR value. This, again, emphasizes that, beyond signaling the edge states, the IPR is not a good tool for probing localization in a quasicrystal in contrast to the quantum metric.